



**HAL**  
open science

# Constitutive model for soil-rock mixtures in the light of an updated skeleton void ratio concept

Tao Wang, Sihong Liu, Antoine Wautier, François Nicot

## ► To cite this version:

Tao Wang, Sihong Liu, Antoine Wautier, François Nicot. Constitutive model for soil-rock mixtures in the light of an updated skeleton void ratio concept. *Acta Geotechnica*, 2023, 18, pp.2991-3003. 10.1007/s11440-022-01756-6 . hal-03852498

**HAL Id: hal-03852498**

**<https://hal.inrae.fr/hal-03852498v1>**

Submitted on 15 Nov 2022

**HAL** is a multi-disciplinary open access archive for the deposit and dissemination of scientific research documents, whether they are published or not. The documents may come from teaching and research institutions in France or abroad, or from public or private research centers.

L'archive ouverte pluridisciplinaire **HAL**, est destinée au dépôt et à la diffusion de documents scientifiques de niveau recherche, publiés ou non, émanant des établissements d'enseignement et de recherche français ou étrangers, des laboratoires publics ou privés.



Distributed under a Creative Commons Attribution 4.0 International License



21 **Abstract:** As a type of special geological body, soil-rock mixtures (SRMs) are widely found in  
22 nature and used in civil engineering. Many structures, such as rockfill dams, highways and tunnels  
23 have used SRMs as building materials. Proper modelling of SRMs is of great importance to  
24 capture the complex behavior of this heterogeneous material. In this manuscript, a simple  
25 constitutive model incorporating the skeleton void ratio concept is proposed for SRMs with  
26 varying soil contents ( $sc$ ). A prominent feature of the model is a unified description of the  
27 behavior of SRMs with varying  $sc$  such that only model parameters of pure rock and of pure soil  
28 are required. After calibration, the model shows a good capacity to predict the stress-strain  
29 response of SRMs under a wide range of  $sc$ , void ratios, and confining pressures. In particular, it  
30 captures well the non-associated behavior of rock-dominated SRMs with different  $sc$ . Furthermore,  
31 the  $sc$ -value is shown to modify the plastic flow direction of the material without influencing its  
32 yield surface.

33 **Keywords:** Soil-rock mixture; Skeleton void ratio; Soil content; Constitutive modelling; Critical  
34 state line; Flow rule direction; Non-associated behavior

## 35 **1. Introduction**

36 Soil-rock mixtures (SRMs) are heterogeneous materials composed of high-strength rocks,  
37 fine-grained soils and pores [37, 38, 42]. SRMs are widely encountered in geotechnical  
38 engineering, such as natural slopes [6], waste rocks and tailings from mining [8], clay-aggregate  
39 mixtures in rockfill dams [12] and tunnels [14]. The soil content ( $sc$ ) is one of the most important  
40 factors governing the mechanical behavior of SRMs [3, 26, 29, 33, 36]. In recent years, many field  
41 tests, laboratory tests and numerical simulations have revealed that  $sc$  greatly affects the shear

42 strength [4, 16, 23, 37], failure modes [5, 15, 17], stress-dilatancy [4, 33], and critical state  
43 parameters of SRMs [25, 33]. Experimental and numerical results both show that at a low  $sc$ , the  
44 mechanical behavior of SRMs is primarily governed by inter-granular friction between rock grains.  
45 While at a high  $sc$  beyond a threshold value  $(sc)_{th}$ , the mechanical behavior of SRM is primarily  
46 governed by friction characteristics of soil grains.

47 Although some pioneering works has been done on the constitutive modelling of SRMs [7,  
48 17, 26], properly modeling the behavior of this kind of complex heterogeneous materials remains  
49 an open challenge [35, 39, 40]. Predicting the mechanical properties SRMs for varying  $sc$  remains  
50 a widely open issue.

51 1) In most constitutive models, SRMs with different  $sc$  are indeed treated as different  
52 materials with their own  $sc$ -specific parameters [21, 24, 41]. For example, the shape of the critical  
53 state line (CSL) of a SRM and its location depend on  $sc$ . Therefore, new laboratory tests are  
54 required each time  $sc$  is updated in engineering projects, which results in a waste of time and  
55 money.

56 2) Some models tried to build empirical equations to link model parameters with  $sc$  [23, 35].  
57 For instance, some empirical equations have been established to fit CSLs of SRMs with  $sc$  based  
58 on experimental data. This method usually introduces new parameters into the constitutive model,  
59 i.e., parameters in empirical equations. But, these empirical equations lack of physical meaning  
60 and their application to SRMs with different lithology, grain shape and gradation of rock and soils  
61 remains questionable.

62 3) Although many numerical studies have analyzed the microstructure of SRMs, few  
63 attempts have been made to incorporate micro- or meso-mechanisms into constitutive models. For

64 example, Wang et al (2021) [29] found that for rock-dominated SRMs,  $sc$  does not affect the  
65 normal direction of yield surface but it changes the flow rule direction. These findings could be  
66 reflected in constitutive models.

67 In soil constitutive models, the global void ratio  $e$  has been chosen as one of the main state  
68 variable. However, it was found to be an imperfect index to characterize the mechanical behavior  
69 of mixed soils like SRMs [29, 33]. This is because such a global index is not able to account for  
70 the non-active participation of the soil grains in the force transmission structure within a SRM.  
71 Alternatively, skeleton void ratio turns out to be a more appropriate index to reflect the density of  
72 SRMs. Skeleton void ratio corresponds to the void ratio of grains constituting the stress-bearing  
73 skeleton. In recent studies, this index has shown a strong potential to give unified descriptions of  
74 the behavior of SRMs with varying  $sc$  [29, 35].

75 The objective of this manuscript is to propose a simple method to predict the stress-strain  
76 response of SRMs with varying  $sc$  incorporating the updated skeleton void ratio concept. It is  
77 organized as follows. First, the updated skeleton void ratio for SRMs proposed by Wang et al.  
78 (2022) [29] is briefly reviewed. The advantage of using this skeleton void ratio index to  
79 characterize critical state lines of SRMs with varying  $sc$  is then shown. Next, a constitutive model  
80 incorporating the skeleton void ratio concept is proposed and the model is validated against  
81 experimental results. Eventually, effect of  $sc$  on the main properties of SRMs is studied and the  
82 model capabilities are discussed.

## 83 **2. Review of an updated skeleton void ratio for SRMs**

84 Wang et al. (2022) [29] proposed an updated skeleton void ratio index for SRMs. The main  
85 advantage of this updated skeleton void ratio is that it can consider the effect of gradations of both

86 soils and rocks. The skeleton void ratio proposed by Thevanayagam (2007) [27] is a special case  
 87 of the updated skeleton void ratio in which mutual interaction between rock and soil grains during  
 88 packing is neglected.

89 According to Wang et al. (2022) [29], the threshold soil content  $(sc)_{th}$  that separates the  
 90 rock-dominated structure and soil-dominated structure is:

$$(sc)_{th} = \frac{e_r - b}{1 + e_r + e_s - a - b} \quad (1)$$

91 where  $e_s$  and  $e_r$  are the minimum void ratios of pure soil grains and pure rock grains,  
 92 respectively.  $a$  and  $b$  are gradation-related parameters:

$$a = (1 + e_s) \exp\left(\frac{-R_d^{0.5}}{C_{ur} C_{us}}\right) \quad (2)$$

$$b = e_r \exp\left(\frac{-R_d}{C_{ur} C_{us}^{0.5}}\right) \quad (3)$$

93 where  $C_{ur} = \frac{(D_{60})_{rock}}{(D_{10})_{rock}}$  is the coefficient of non-uniformity for the rock fraction,  $C_{us} = \frac{(d_{60})_{soil}}{(d_{10})_{soil}}$  is  
 94 the coefficient of non-uniformity for the soil fraction and  $R_d = \frac{(D_{50})_{rock}}{(d_{50})_{soil}}$  is grain size disparity  
 95 ratio.

96 For a rock-dominated structure, i.e.,  $sc < (sc)_{th}$ , its skeleton void ratio  $e_{sk}$  is given by:

$$e_{sk} = \frac{e + sc}{1 - sc} - \frac{sc(1 + e_s)}{1 - sc} \exp\left(\frac{-R_d^{0.5}}{C_{ur} C_{us}}\right) \quad (4)$$

97 For a soil-dominated structure, i.e.,  $sc > (sc)_{th}$ , its skeleton void ratio  $e_{sk}$  expresses as:

$$e_{sk} = \frac{e}{sc} - \frac{e_r(1 - sc)}{sc} \exp\left(\frac{-R_d}{C_{ur} C_{us}^{0.5}}\right) \quad (5)$$

98 All the parameters introduced in Equations (1)-(5) can be obtained from simple laboratory  
 99 sieving and compaction tests.

100 Wang et al. (2022) [29] found that a rock-dominated (or soil-dominated) SRM has similar  
 101 stress-strain responses with a pure rock specimen (or a pure soil specimen) if global void ratio of

102 the pure rock specimen (or pure soil specimen) equals to the skeleton void ratio of the SRM. This  
103 important finding is essential to unify descriptions of SRMs with varying soil contents.

### 104 **3. Characterization of critical state lines of SRMs with** 105 **updated skeleton void ratio index**

106 The critical state is defined as the state at which the soil continues to deform at constant shear  
107 stress and constant volume. It has increasingly been used as a fundamental concept to characterize  
108 the strength and deformation properties of soils [2, 20, 22]. Li et al. (1998) [10] found that the  
109 critical state lines (CSLs) for cohesionless soils are straight lines in the  $e-(p/p_a)^\xi$  plane:

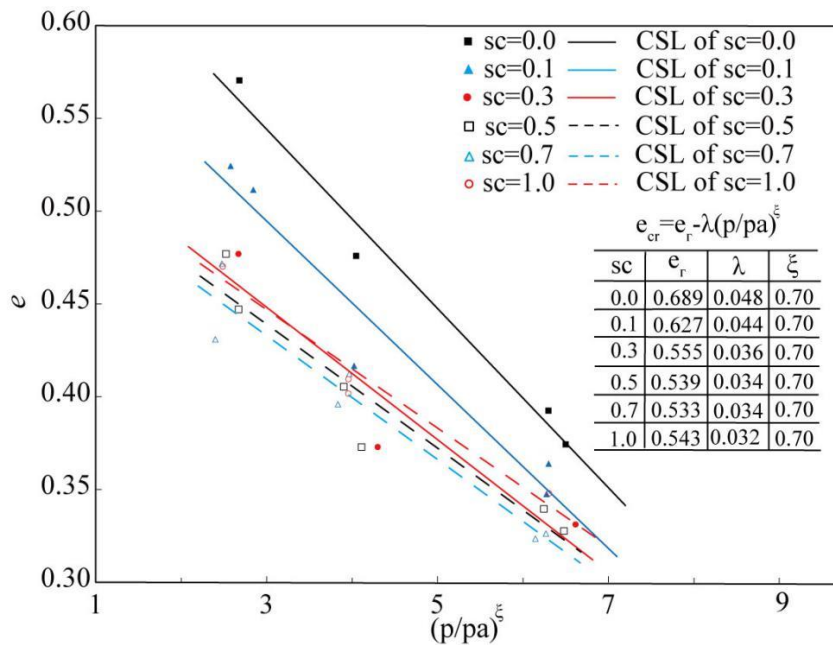
$$e_{cr} = e_\Gamma - \lambda(p/p_a)^\xi \quad (6)$$

110 Where  $e_{cr}$  is critical state void ratio,  $e_\Gamma$  is the theoretical critical void ratio at the atmospheric  
111 pressure,  $p_a$  is the atmospheric pressure,  $\lambda$  is the magnitude of the slope, and  $\xi$  is the pressure  
112 exponent (with a typical value around 0.7).

113 Experimental data obtained from conventional drained triaxial tests on SRMs with different  
114 soil contents ( $sc=0, 0.1, 0.3, 0.5, 0.7$  and  $1$ ) under different confining pressures ( $\sigma_3=150$  kPa,  $300$   
115 kPa and  $600$  kPa) conducted by Wang et al. (2022) [29] are adopted here to characterize the CSLs  
116 of SRMs with varying  $sc$  ( $C_{ur} = 2.36$ ,  $C_{us} = 7.01$  and  $R_d=5.46$ ). Detailed test procedures can be  
117 found in the quoted reference [29].

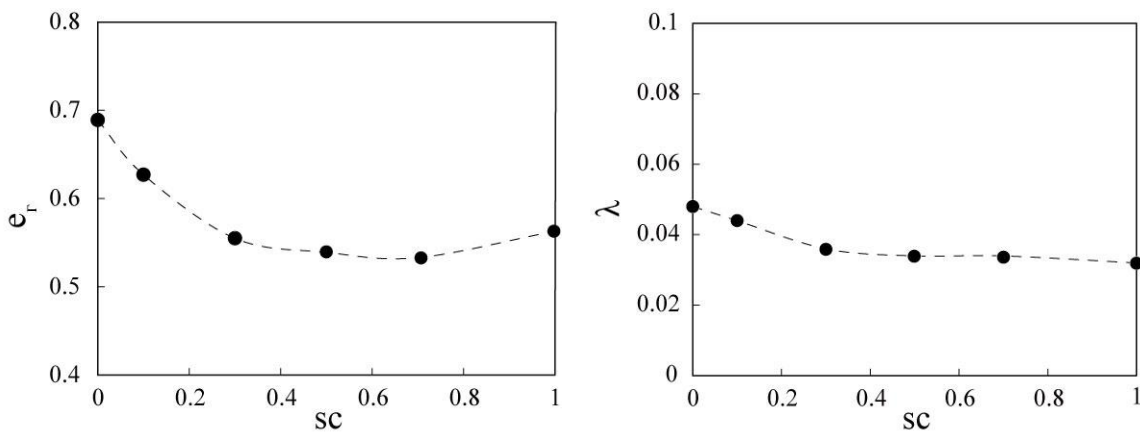
118 Figure 1 gives the CSLs of SRMs with  $sc$  ranging from  $0$  to  $1$  in  $e-p$  plane. It can be found  
119 that SRMs with different  $sc$  have different CSLs. The CSL move downward from the pure rock  
120 specimen until the soil content reaches  $(sc)_{th}$  (around  $0.54$ ), and then the CSL would move  
121 upward to the position of pure soil specimen. According to Wang et al. (2022), all the SRMs were  
122 prepared with the same global void ratio. For a rock-dominated specimen, the skeleton void ratio

123 increases with  $sc$  and a more contractant behavior is observed. Therefore, the increase in  $sc$  widens  
 124 the gap between current void ratio and critical void ratio and leads to the downward shift of the  
 125 CSL. On the other hand, for a soil-dominated specimen, the increase in  $sc$  results in a larger  
 126 skeleton void ratio and a more dilatant behavior, which consequently narrows the gap. Therefore,  
 127 CSL will move upwards. Critical state line parameters  $e_r$  and  $\lambda$  are shown in Figure 2.  $e_r$  and  
 128  $\lambda$  are found to be functions of  $sc$ , which indicates that SRMs with different  $sc$  should be treated as  
 129 different materials. Consequently, each SRM has its own CSL in  $e-p$  plane.



130  
 131  
 132  
 133

**Fig. 1 Critical state lines of SRMs with different  $sc$  drawn in  $e-(p/p_a)^\xi$  plane**



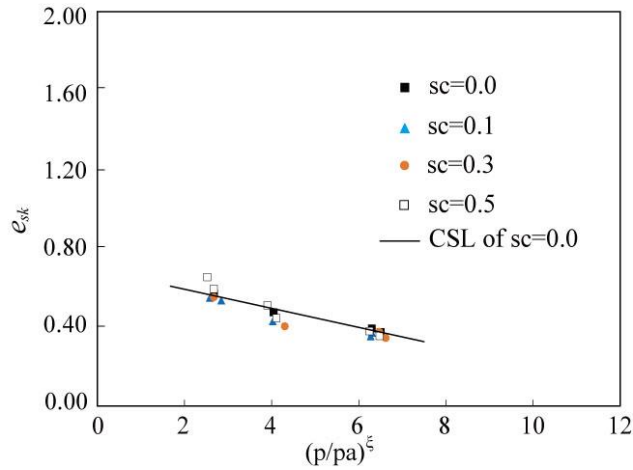


(a)  $e_{\Gamma}$

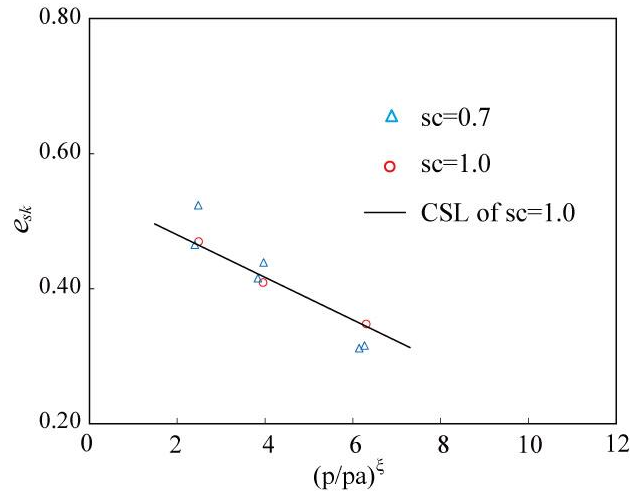
(b)  $\lambda$

**Fig. 2 Evolution of critical state parameters with  $sc$ : (a)  $e_{\Gamma}$ ; (b)  $\lambda$**

134 Critical state data of SRMs with different  $sc$  are plotted in  $e_{sk}-p$  plane in Figure 3. Pure rock  
135 and pure soil materials have different CSLs because they have different grain shapes and  
136 gradations. Therefore, for a clearer view, we plot separately the critical state data of  
137 rock-dominated structure (Figure 3a) and soil-dominated structure (Figure 3b). It can be seen in  
138 Figure 3a, that the CSL of pure rock grains ( $sc=0$ ) is shared with SRMs of different  $sc$  ( $sc=0, 0.1,$   
139  $0.3$  and  $0.5 < (sc)_{th} = 0.54$ ) for rock-dominated SRMs. Similarly, as shown in Figure 3b, for the  
140 soil-dominated specimens ( $sc=0.7, 1 > (sc)_{th} = 0.54$ ), the CSL of the pure soil ( $sc=1$ ) is shared with  
141 SRM with  $sc=0.7$ . Consequently, in the  $e_{sk}-p$  plane, the critical state of all RSM materials is  
142 described either by the CSL of the rock or the SCL of the soil depending whether  $sc$  is below or  
143 above  $(sc)_{th}$ . This important finding is essential for establishing the constitutive model, as  
144 developed in the next section.



**(a) Rock-dominated SRMs**



(b) Soil-dominated SRMs

Fig. 1 Critical state lines of SRMs with different  $sc$  drawn in  $e_{sk} - (p/p_a)^\xi$  plane

## 145 4. A simple constitutive model for SRM using the skeleton 146 void ratio index

147 The updated skeleton void ratio concept is incorporated into the state-dependent bounding  
148 surface model proposed by Li and Dafalias (2000) [9] to capture the stress-strain behaviors of  
149 SRMs with different  $sc$ . The fundamental of this model is that the SRMs and its host rock (or soil)  
150 with the same skeleton void ratio should exhibit the same stress-strain behavior, which has been  
151 reported by many researchers [28, 29, 35]. The fact that rock-dominated (or soil-dominated)  
152 SRMs share the same CSL with pure rock (or pure soil) also suggests to build a unified model for  
153 SRMs with varying  $sc$  from only model parameters of pure rock and pure soil. The constitutive  
154 framework is detailed in the following sections.

### 155 4.1 Elastic behavior

156 According to standard elasto-plasticity, a total strain increment  $d\boldsymbol{\varepsilon}$  is additively split into an  
157 elastic strain increment  $d\boldsymbol{\varepsilon}^e$  and a plastic strain increment  $d\boldsymbol{\varepsilon}^p$ :

$$d\boldsymbol{\varepsilon} = d\boldsymbol{\varepsilon}^e + d\boldsymbol{\varepsilon}^p \quad (7)$$

158 The volumetric and deviatoric elastic strain increments are given respectively by:

$$d\varepsilon_v^e = \frac{dp'}{K} \quad (8)$$

$$d\varepsilon_d^e = \frac{dq}{3G} \quad (9)$$

159 where  $K$  is the elastic bulk modulus,  $G$  is the elastic shear modulus,  $p' = \frac{\sigma_1 + 2\sigma_3}{3}$  is the mean  
160 effective stress and  $q = \sigma_1 - \sigma_3$  is the deviatoric stress ( $\sigma_1$ ,  $\sigma_2$ , and  $\sigma_3$  are the principal stress  
161 values).

162  $G$  can be estimated following [19]:

$$G = G_0 \frac{(2.97 - e)^2}{(1 + e)} \sqrt{p' p_a} \quad (10)$$

163 where  $G_0$  is an elastic material constant,  $p_a$  is the atmospheric pressure,  $e$  is the void of the  
164 considered material (soil or rock).

165 The elastic bulk modulus  $K$  is given by the following relation:

$$K = G \frac{2(1+\nu)}{3(1-2\nu)} \quad (11)$$

166 where  $\nu$  is the Poisson's ratio.

167 The estimation of  $G_0$  and  $\nu$  can be found in Appendix.

## 168 4.2 Plastic behavior

169 For the sake of simplicity, the elasto-plastic model proposed by Li and Dafalias (2000) [9] in  
170 the triaxial compression stress space is adopted. In this model, the yield surface is given by:

$$f(p', q, \eta) = q - p' \eta_c = 0 \quad (12)$$

171 where  $\eta_c$  is the stress ratio when plasticity activates. In the model of Li and Dafalias (2000) [9]  
172 the yield surface is assumed to follow the stress state so that  $\eta_c = \eta$ . Note that this hypothesis  
173 holds as long as plasticity is activated. In case elastic unloading is considered, the model requires  
174 some additional mechanism such as a back-stress [13], or a memory of the reversal stress ratio

175 point [31] which are not considered in the present study.

176 According to the theory of plasticity, a loading index  $dL$  can be defined as:

$$dL = \frac{1}{K_p} \left( \frac{\partial f}{\partial p'} dp' + \frac{\partial f}{\partial q} dq \right) = \frac{dq - \eta_c dp'}{K_p} = \frac{p' d\eta}{K_p} \quad \text{since } \eta_c = \eta \quad (13)$$

177 where  $K_p$  is the plastic hardening modulus and is expressed by Li and Dafalias (2000) [9] as:

$$K_p = hG \left( \frac{M}{\eta} - \exp(n\psi) \right) = \frac{hG \exp(n\psi)}{\eta} (M \exp(-n\psi) - \eta) \quad (14)$$

178 In the above equation,  $n$  is a positive model parameter,  $h = h_1 - h_2 e_0$  with  $h_1$  and  $h_2$  are

179 model parameters and  $e_0$  the initial void ratio,  $M$  is the stress ratio at a critical state and

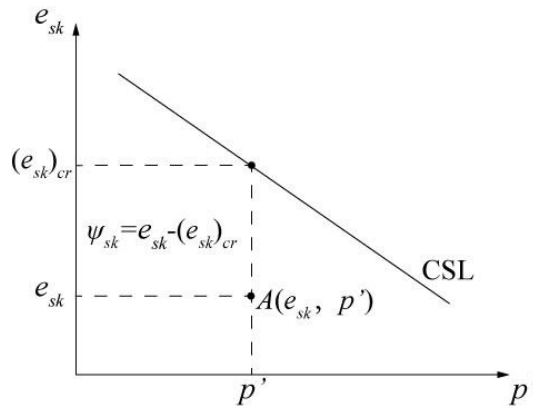
180  $\psi = e - e_{cr}$  is the state parameter defined by Been and Jefferies (1985) [1] with  $e$  the current

181 void ratio and  $e_{cr}$  the critical state void ratio for the current  $p'$ . When using skeleton void ratio

182 instead of the void ratio, a skeleton state parameter  $\psi_{sk}$  is introduced as  $\psi_{sk} = e_{sk} - (e_{cr})_{sk}$ , as

183 seen in Figure 4. Note that when softening occurs ( $K_p < 0$ ) the plastic multiplier  $dL$  is positive

184 (i.e. plasticity is active) when the stress ratio decreases.



185

186

**Fig. 4 Definition of skeleton state parameter  $\psi_{sk}$**

187 Since soil-rock mixtures are typical non-associated materials, the non-associated flow rule is

188 adopted to define the plastic strain increments, as follows:

$$d\varepsilon_d^p = dL = \frac{p' d\eta}{K_p} \quad (15)$$

$$d\varepsilon_v^p = DdL = \frac{Dp' d\eta}{K_p} \quad (16)$$

189 where  $d\varepsilon_d^p$  and  $d\varepsilon_v^p$  are the plastic deviatoric strain increment and the plastic volumetric strain  
 190 increment, respectively. The ratio  $D = \frac{d\varepsilon_v^p}{|d\varepsilon_d^p|}$  evaluates the amplitude of the dilatancy and can be  
 191 chosen as follows:

$$D = \frac{d_0}{M} [M \exp(m\psi) - \eta] \quad (17)$$

192 where  $d_0$  and  $m$  are model parameters. For associated flow rule,  $D = \frac{d\varepsilon_v^p}{d\varepsilon_d^p} = \frac{\frac{\partial f}{\partial p}}{\frac{\partial f}{\partial q}} = -\eta_c$ .

193 Therefore, for  $dL > 0$ , the following expressions can be derived for both incremental deviatoric  
 194 and volumetric strains:

$$d\varepsilon_d = d\varepsilon_d^e + d\varepsilon_d^p = \frac{dq}{3G} + \frac{P'd\eta}{K_p} = \left( \frac{1}{3G} + \frac{1}{K_p} \right) dq - \frac{\eta}{K_p} dp' \quad (18)$$

$$d\varepsilon_v = d\varepsilon_v^e + d\varepsilon_v^p = \frac{dp'}{K} + D d\varepsilon_d^p = \frac{D}{K_p} dq + \left( \frac{1}{K} - \frac{D\eta}{K_p} \right) dp' \quad (19)$$

195 Equations (18) and (19) set up the relationship between strain and stress increments.  
 196 Eventually, an elastoplastic constitutive relation is derived in a matrix form:

$$\begin{Bmatrix} dq \\ dp' \end{Bmatrix} = \left[ \begin{pmatrix} 3G & 0 \\ 0 & K \end{pmatrix} - \frac{h(dL)}{K_p + 3G - K\eta D} \begin{pmatrix} 9G^2 & -3KG\eta \\ 3KGD & -K^2\eta D \end{pmatrix} \right] \begin{Bmatrix} d\varepsilon_d \\ d\varepsilon_v \end{Bmatrix} \quad (20)$$

197 where  $h(dL)$  is a Heaviside function with  $h(L)=1$  for  $dL > 0$  and  $h(dL)=0$ , otherwise (plastic stain  
 198 exists only when  $dL$  is positive). Note that equation (20) is given in the plane  $(dp', dq)$  and the  
 199 dual plane  $(d\varepsilon_v, d\varepsilon_d)$ . It can be generalized to any kind of incremental stress and strain tensors by  
 200 assuming coaxiality between incremental stress and strain.

### 201 4.3 Model parameters

202 To summarize, the proposed model includes eleven model parameters, all of them being  
 203 calibrated from drained triaxial tests under different confining pressures: (1) Two elastic  
 204 parameters, i.e.  $G_0$  and  $\nu$ ; (2) Four critical state parameters, i.e.  $M$ ,  $e_\Gamma$ ,  $\lambda$  and  $\xi$ ; (3) Two  
 205 dilatancy parameters, i.e.  $d_0$ ,  $m$ ; (4) Three hardening parameters, i.e.  $h_1$ ,  $h_2$  and  $n$ .

206 It should be noted that no new parameters have been introduced into this approach. Skeleton

207 void ratio  $e_{sk}$  of SRMs with different  $sc$  are adopted to replace global void ratio  $e$  in the  
 208 above-mentioned equations. Accordingly, skeleton state parameter  $\psi_{sk}$  is used in the place of  $\psi$ .  
 209 By doing so, the behavior of SRMs with varying  $sc$  can be predicted from only the model  
 210 parameters of pure rock and pure soil. Thus, SRMs with different  $sc$  should no longer be treated as  
 211 different materials and only require own  $sc$ -specific model parameters.

## 212 **5. Model performance**

213 In this section, the experimental data obtained by Wang et al. (2022) [29] are adopted to test  
 214 the performance of the constitutive model introduced above. In reference [29], conventional  
 215 drained triaxial tests on soil-rock mixtures with  $sc=0, 0.1, 0.3, 0.5, 0.7$  and  $1$  were conducted  
 216 under three different confining pressures ( $\sigma_3=150$  kPa,  $300$  kPa and  $600$  kPa).

217 The threshold soil content  $(sc)_{th}$  of the SRM used in [26] is  $0.54$ . The threshold soil  
 218 content is larger than that reported by other researchers. The reason may be the use of angular  
 219 gravel in their tests, which cause large voids among rock grains. Therefore, SRMs with  $sc=0.1, 0.3$   
 220 and  $0.5$  are rock-dominated SRMs, whose behavior can be predicted from model parameters of  
 221 pure rock, while stress-strain responses of soil-dominated SRM (i.e.,  $sc=0.7$ ) can be predicted  
 222 from the model parameters of pure soil. The calibrated model parameters of the pure rock and  
 223 pure soil used in [26] are listed in Table 1. The description of the calibration process of model  
 224 parameters is reported in Appendix.

225

226 **Table 1. Model parameters calibrated for pure rock ( $sc=0$ ) and pure soil ( $sc=1$ ).**

Elastic parameters	Critical state parameters	Dilatancy parameters	Hardening parameters
--------------------	---------------------------	----------------------	----------------------

Pure rock ( $sc=0$ )	$G_0 = 200$	$M = 1.79$	$d_0 = 1.5$	$h_1 = 0.2$
	$\nu = 0.32$	$e_\Gamma = 0.689$	$m = -1.0$	$h_2 = 0.3$
		$\lambda = 0.048$		$n = 3.9$
		$\xi = 0.70$		
Pure soil ( $sc=1$ )	$G_0 = 50$	$M = 1.70$	$d_0 = 1.8$	$h_1 = 0.6$
	$\nu = 0.25$	$e_\Gamma = 0.543$	$m = 0.2$	$h_2 = 2.0$
		$\lambda = 0.032$		$n = 7.0$
		$\xi = 0.70$		

## 227 5.1 Stress-strain-volume behavior

228 Figures 5 and 6 display comparisons between predicted results and experimental results in  
229 terms of stress ratios, volumetric strains and evolutions of global void ratios for SRMs with  
230 varying  $sc$ . It can be seen that the stress ratio and the volumetric strain can be fairly described by  
231 the model for drained shear responses of SRMs under a range of confining stresses and soil  
232 contents.

233 SRMs exhibit post peak strain softening and volumetric expansion at a low confining  
234 pressure i.e.,  $\sigma_3=150$  kPa. While at higher confining pressures, i.e.,  $\sigma_3=300$  kPa and 600 kPa,  
235 SRMs present strain hardening and the volumetric contraction. As shown in Figure 5, the model  
236 can capture both the stress and the volumetric strain behaviors of SRMs with varying  $sc$ , e.g., the  
237 strain hardening, the volumetric contraction, the strain softening, and the volumetric expansion. In  
238 addition, the predicted peak stress ratio, critical stress ratio, phase transformation point from  
239 contraction to dilatancy, ultimate volumetric strain, and evolution of void ratio agree well with  
240 experimental results.

241 Some discrepancies between simulated and experimental curves may be observed when  $sc$  is  
242 close to  $(sc)_{th}$ , i.e., when  $sc=0.3$  and 0.5. One possible reason for this phenomenon is that when  $sc$   
243 is close to  $(sc)_{th}$  a dual skeleton structure is formed in SRM which is composed of both rock and

244 soil grains. Therefore, some discrepancies may occur if we still regard the SRMs as pure

245 rock-skeleton structure or soil-skeleton structure.

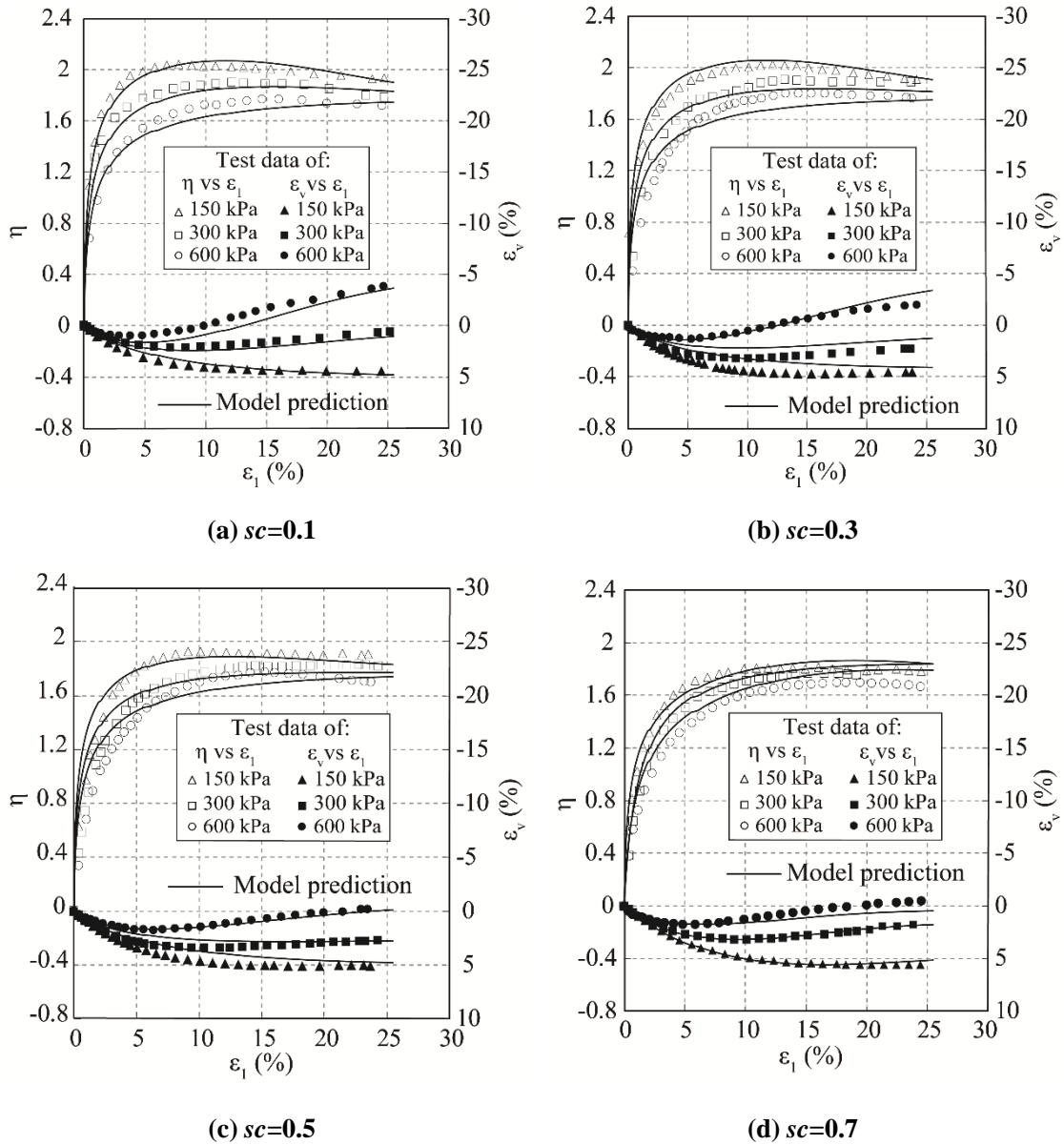


**Fig. 5 Comparison between predicted results and experimental results in terms of stress ratio versus axial strain and volumetric strain versus axial strain.**



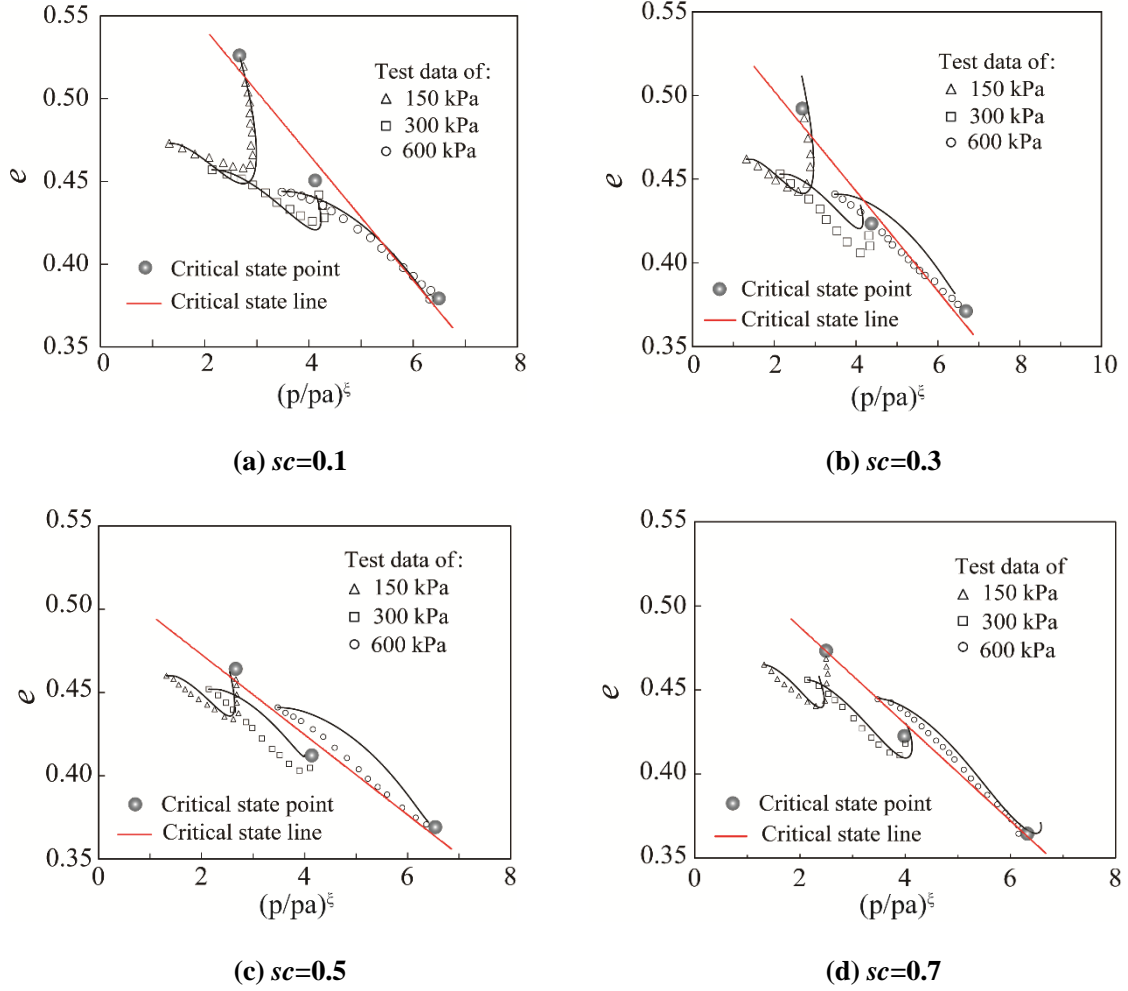


**Fig. 6 Comparison between predicted results and experimental results in terms of void ratio versus mean pressure**

## 246 **5.2 Mobilized friction angle**

247 In this section, we assess whether our model can properly reflect the mobilized friction angle  
 248 of SRMs with different  $sc$  and confining pressures. The mobilized friction angle  $\varphi_m$  is defined as:

$$\sin\varphi_m = \frac{\sigma_1 - \sigma_3}{\sigma_1 + \sigma_3} \quad (21)$$

249 where  $\sigma_1$  and  $\sigma_3$  are major and minor principal stresses, respectively. In axisymmetric

250 conditions,  $\sin\varphi_m = \frac{3\eta}{6+\eta}$ .

251 Figure 7 shows the comparisons between test results and model predictions in terms of the

252 relationship between mobilized friction angle  $\varphi_m$  and void ratio  $e$ . It can be seen that the model

253 captures well the variations of  $\varphi_m$  with  $e$  for SRMs under different confining pressures, although

254 the model slightly overestimates  $\varphi_m$  at high confining pressure of 600 kPa when  $sc=0.3$  and  $0.5$ .

255 This might be due to the formation of a dual skeleton structure in the specimen with both rock and

256 soil grains when  $sc=0.3$  and  $0.5$  (close  $(sc)_{th} = 0.54$ ).

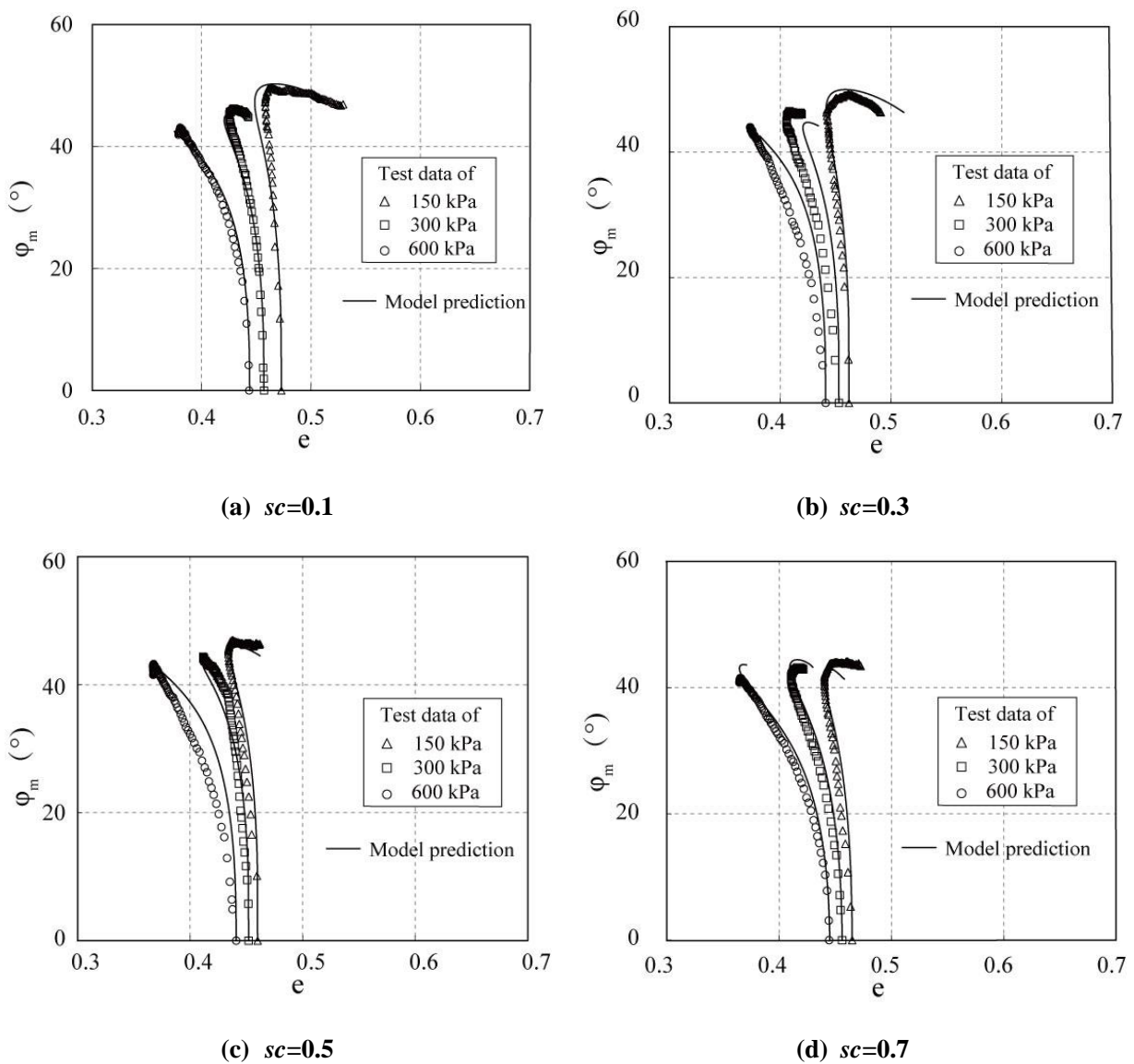


**Fig. 7 Comparison between predicted results and experimental results in terms of void ratio versus mobilized friction angle  $\varphi_m$ .**

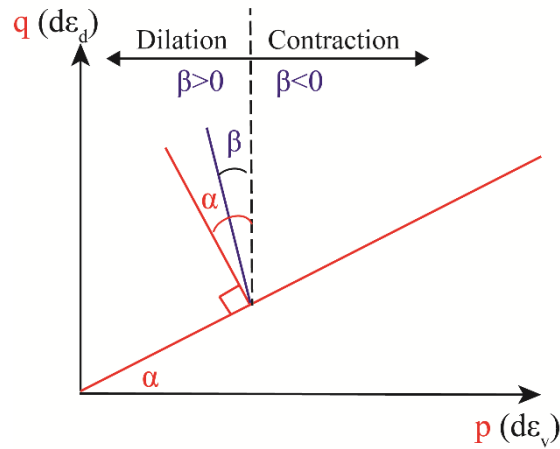
257 **6. Effect of soil content on essential behavior of SRMs**

258 **6.1 Effect of  $sc$  on the non-associate behavior**

259 In order to investigate the effect of  $sc$  on the non-associated behavior of rock-dominated  
 260 SRMs, the yield surface normal direction  $\alpha$  and flow rule direction  $\beta$  can be introduced as  
 261 illustrated in Figure 8 in the  $p$ - $q$  plane and dual  $d\varepsilon_v$ - $d\varepsilon_d$  plane for a non-associated flow rule with  
 262 on a yield surface corresponding to Mohr-Coulomb criterion.

$$\tan\alpha = \frac{q}{p} \quad (22)$$

$$\tan\beta = -\frac{d\varepsilon_v}{d\varepsilon_d} \quad (23)$$

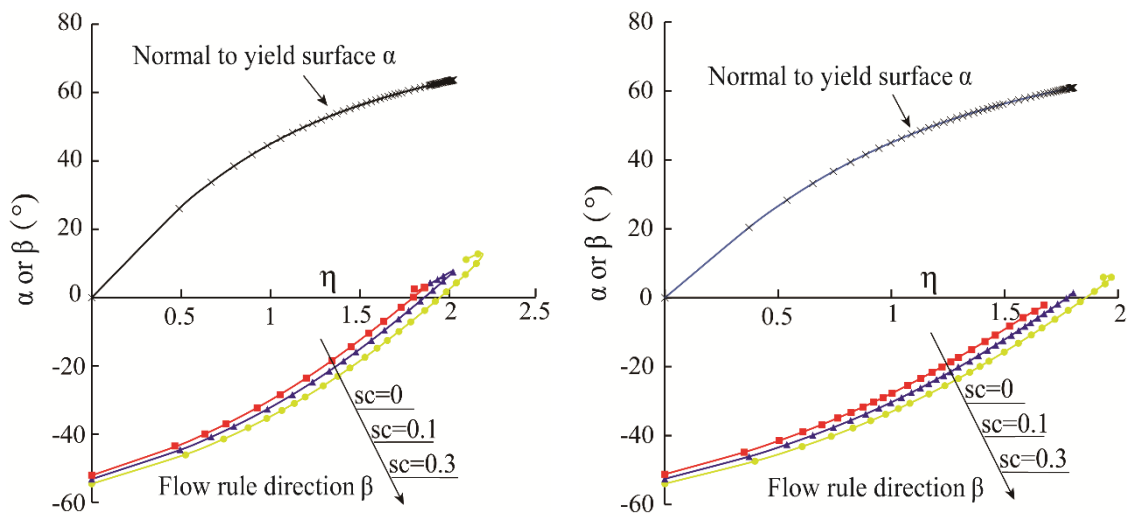


263 **Fig. 8 Schematic diagram of normal to yield surface and flow rule direction. Both directions**  
 264 **can be formulated with respect to angles  $\alpha$  and  $\beta$ . The sign convention of soil mechanics is**  
 265 **applied (positive stress in compression and positive strain in contraction).**  
 266

267

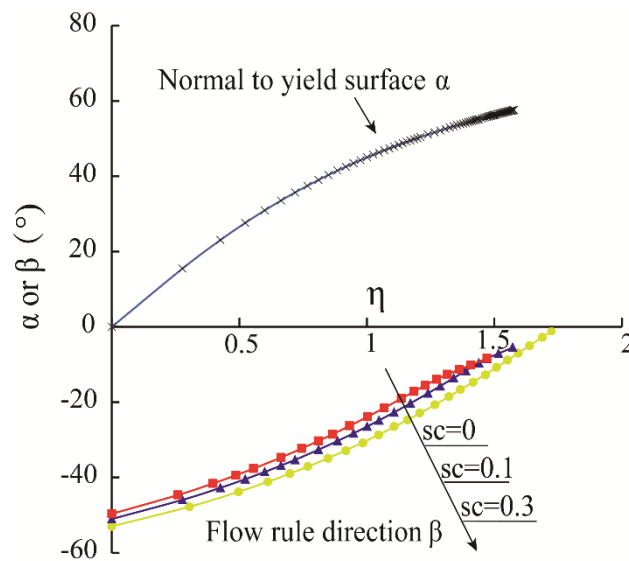
268 Knowing the model yield function from equation (12), the normal direction to the yield  
 269 surface  $\alpha$  and flow rule direction  $\beta$  are shown in Figure 9 for rock-dominated SRMs ( $sc=0, 0.1$

270 and 0.3) under confining pressures of 150 kPa, 300 kPa and 600 kPa. It can be seen that for each  
 271 confining pressure, when compared at the same stress ratio  $\eta$ ,  $\alpha$  of SRMs with different  $sc$  are the  
 272 same, indicating a non-dependence of the normal yield surface direction upon  $sc$ . On the other  
 273 hand,  $\beta$  increases with  $sc$  (positive for dilation and negative for contraction), indicating that  
 274 SRMs exhibit more dilatancy with the increase of  $sc$ . Therefore, the angle between normal  
 275 direction of yield and flow rule direction decreases with  $sc$ , meaning the non-associate character is  
 276 less pronounced with  $sc$ .



(a)  $\sigma_3=150$  kPa

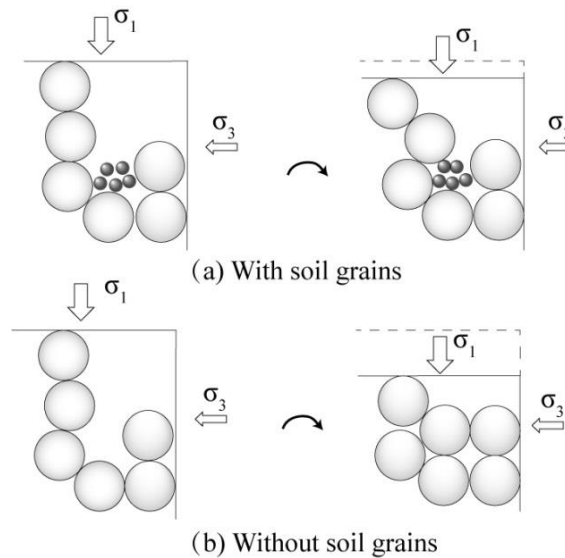
(b)  $\sigma_3=300$  kPa



(c)  $\sigma_3=600$  kPa

**Fig. 9 Normal to yield surface and flow rule direction of rock-dominated SRMs with  $sc=0, 0.1$  and  $0.3$  under confining pressure of 150 kPa, 300 kPa and 600 kPa.**

277 The mesoscale origin of plastic deformation in SRMs is illustrated in Figure 10. The  
278 macroscopic activation of the plastic behavior corresponds to substantial grain rearrangements  
279 resulting from the collapse of preexisting force chains oriented in the principal stress direction (the  
280 vertical direction in Figure 10). Once they collapse, the specimen shrinks in this direction together  
281 with smaller expansion in the lateral direction. When small grains fill the pore space, the vertical  
282 contraction decreases, whereas the lateral expansion is mostly unaffected. Therefore, the increase  
283 in soil content is expected to enhance dilatancy in SRMs specimens.



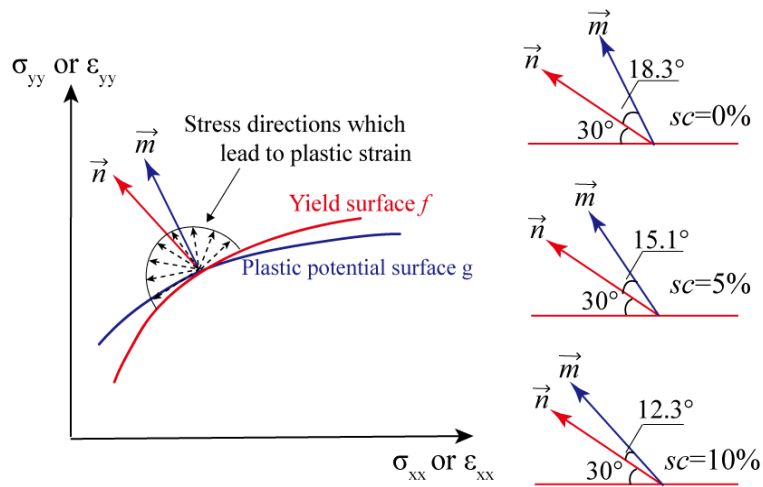
284

285 **Fig. 10** Illustration of the plastic deformation with and without soil grains [29]

286 The conceptual model of Figure 10 was proved with DEM results by Wang et al. (2021) [29]  
287 and Wautier et al. (2019) [32]. Wang et al. (2021) [29] found that for rock-dominated SRMs,  $sc$   
288 does not affect the normal direction of yield surface but it changes the flow rule direction. For  
289 rock-dominated SRMs, the non-associated character is less pronounced with the increase of  $sc$ , as

290 shown in Figure 11. It should be noted that the normal directions of yield and plastic potential  
 291 surfaces shown in Fig. 11 are computed directly from DEM results, while the normal to yield  
 292 surface in Figure 9 depends on the expression of yield surface selected (e.g., Equation (12)).

293 Similarly, in the proposed model, soil content is found to affect the flow rule direction but the  
 294 mechanical state and the yield surface of rock-dominated SRMs are not affected. Indeed, this is an  
 295 intrinsic property of the elasto-plastic model of Li and Dafalias (2000) [9] used in this study. The  
 296 model assumes that the yield surface follows the stress state at any time (see Equation 12 where  
 297 the current stress ratio is used). Consequently, the yield surface is independent of the soil content.  
 298 The consistency between model predictions and DEM simulations proves the ability of this  
 299 constitutive model to properly reflect the non-associated properties of SRMs with  $sc$ .

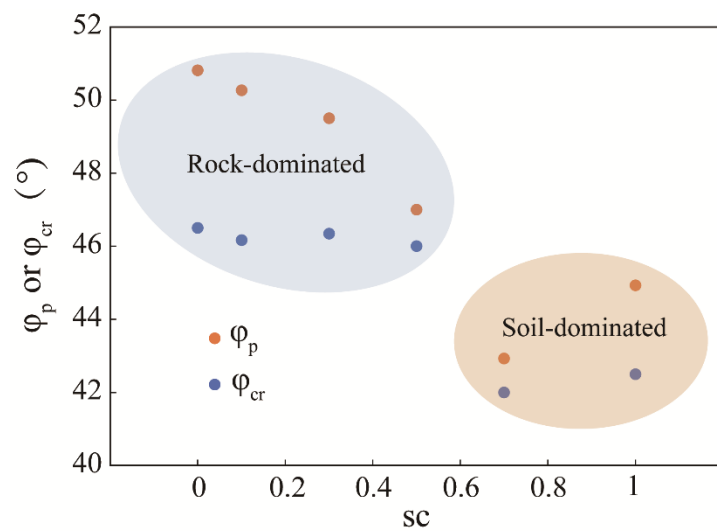


300  
 301 **Fig. 11** Schematic diagram of yield surface  $f$  and plastic potential surface  $g$  (on the left) and their  
 302 normal directions  $\vec{m}$  and  $\vec{n}$  (on the right) for DEM specimens with different  $sc$  at the same stress  
 303 ratio  $\eta=0.43$  (Wang et al., 2021 [29]).

## 304 6.2 Effect of $sc$ on peak and critical state friction angle

305 As can be seen in Figure 7,  $\varphi_m$  increases to a peak value  $\varphi_p$ , i.e., peak friction angle, and

306 then decreases to the critical state friction angle  $\varphi_{cr}$  at relatively low confining pressures. Values  
 307 of  $\varphi_p$  and  $\varphi_{cr}$  of SRMs with varying  $sc$  are displayed in Figure 12. It can be seen that  $\varphi_{cr}$   
 308 almost keeps constant for both rock-dominated structure (at low  $sc$ ) and soil-dominated structure  
 309 (at high  $sc$ ), while  $\varphi_p$  decreases with  $sc$  for rock-dominated structure and increases with  $sc$  for  
 310 soil-dominated structure. For rock-dominated structures, as a rock skeleton exists,  $\varphi_{cr}$  is  
 311 primarily governed by intergranular friction between rock grains. Therefore,  $\varphi_{cr}$  is constant for  
 312 all rock-dominated SRMs. Likewise, for soil-dominated structures, a soil skeleton exists, and  
 313  $\varphi_{cr}$  is primarily governed by friction characteristics of soil grains. Therefore,  $\varphi_{cr}$  is also constant  
 314 for all soil-dominated SRMs. The reason why  $\varphi_{cr}$  in rock-dominated structures is higher than  
 315 that in soil-dominated structures is that the rock grains used in triaxial tests are more angular than  
 316 soil grains. However,  $\varphi_p$  is related to the density (in particular  $e_{sk}$ ) of the initial SRM samples. It  
 317 is reported in [29] that  $e_{sk}$  decreases with  $sc$  for rock-dominated SRMs and increases with  $sc$  for  
 318 soil-dominated SRMs. This explains why  $\varphi_p$  decreases with  $sc$  for rock-dominated SRMs and  
 319 increases with  $sc$  for soil-dominated SRMs.



320

321 **Fig. 12 Changes in peak friction angle  $\varphi_p$  and critical friction angle  $\varphi_{cr}$  with  $sc$**

322

( $\sigma_3=150\text{kPa}$ )

## 323 **7. Closure remarks**

324       The main contribution of this work is the proposal of a simple method to predict the  
325 stress-strain responses of SRMs with varying soil contents. This method incorporates the concept  
326 of an updated skeleton void ratio. Using this concept, SRMs with different  $sc$  should no longer be  
327 regarded as different materials with their own  $sc$ -dependent model parameters. Only model  
328 parameters of pure rock and of pure soil are required to describe the stress-strain response SRMs  
329 with varying  $sc$ . Our proposal to adopt the skeleton void ratio is generic and can be applied to  
330 other constitutive frameworks, ranging from phenomenological models to micro-mechanically  
331 based models provided that skeleton parameters (for instance,  $e_{sk}$  and  $\psi_{sk}$ ) are adopted. In this  
332 manuscript, the constitutive framework proposed by Li and Dafalias (2000) [9] is adopted as an  
333 example to demonstrate the effectiveness of this method. Extending this investigation toward  
334 other constitutive frameworks will be considered in future work.

335       The proposed method demonstrates a satisfying ability for predicting stress-strain responses  
336 of SRMs with different soil contents and confining pressures. In addition, it successfully reflects  
337 the non-associativity behavior of rock-dominated SRMs. Some discrepancies between simulated  
338 and experimental curves are observed when  $sc$  is close to  $(sc)_{th}$ . One possible reason for this  
339 phenomenon is that a dual skeleton structure composed of both rock and soil grains is formed in  
340 SRM when  $sc$  is close to  $(sc)_{th}$ . This could be improved in future work by characterizing the  
341 complex dual skeleton structure in DEM simulations or X-ray tomography images for instance.

## 342 **Acknowledgements**

343       This work was supported by National Natural Science Foundation of China (Grant No.  
344 U1765205 and No. 51979091). The authors also express their sincere thanks to the International



345 Research Network GeoMech (IRN GeoMech, CNRS) for promoting stimulating and convivial  
346 interactions among researchers.

## 347 **References**

- 348 1 Been K, Jefferies MG (1985) A state parameter for soils. *Geotechnique* 35: 99-112
- 349 2 Casagrande A (1936) Characteristics of cohesionless soils affecting the stability of slopes and  
350 earth fills. *J. Boston Society of Civil Engineers* 23:13-32
- 351 3 Cen D, Huang D, Ren F (2017) Shear deformation and strength of the interphase between the  
352 soil–rock mixture and the benched bedrock slope surface. *Acta Geotechnica* 12: 391-413
- 353 4 Chen GX, Wu Q, Sun T, et al (2021) Cyclic behaviors of saturated sand-gravel mixtures under  
354 undrained cyclic triaxial loading. *Journal of Earthquake Engineering* 25:756-789
- 355 5 Dong H, Peng BC, Gao QF, et al (2021) Study of hidden factors affecting the mechanical  
356 behavior of soil–rock mixtures based on abstraction idea. *Acta Geotechnica* 16:595-611
- 357 6 Gao WW, Gao W, Hu RL, et al (2018) Microtremor survey and stability analysis of a soil-rock  
358 mixture landslide: a case study in Baidian town, China. *Landslides* 15:1951-1961
- 359 7 Gobbi, S., Santisi d’Avila, M. P., Lenti, L., Semblat, J. F., & Reiffsteck, P. (2022). Effect of  
360 active plastic fine fraction on undrained behavior of binary granular mixtures. *International*  
361 *Journal of Geomechanics*, 22(1), 06021035.
- 362 8 Khalili A, Wijewickreme D, Wilson GW (2010) Mechanical response of highly gap-graded  
363 mixtures of waste rock and tailings. Part I: Monotonic shear response. *Canadian Geotechnical*  
364 *Journal* 47:52-565
- 365 9 Li XS, Dafalias YF (2000) Dilatancy for cohesionless soils. *Geotechnique* 50: 449-460
- 366 10 Li XS, Wang Y (1998) Linear representation of steady-state line for soil. *Journal of*  
367 *geotechnical and geoenvironmental engineering* 124:1215–121
- 368 11 Liu HB, Zou DG (2013) Associated generalized plasticity framework for modeling gravelly  
369 soils considering particle breakage. *Journal of Engineering Mechanics* 139:606-615
- 370 12 Lu Y, Liu SH, Zhang YG, et al (2021) Hydraulic conductivity of gravelly soils with various  
371 coarse particle contents subjected to freeze–thaw cycles. *Journal of Hydrology* 598:126302
- 372 13 Manzari MT, Dafalias YF (1997) A critical state two-surface plasticity model for  
373 sands. *Geotechnique* 47:255-272
- 374 14 Napoli ML, Barbero M, Scavia C (2021) Tunneling in heterogeneous rock masses with a  
375 block-in-matrix fabric. *International Journal of Rock Mechanics and Mining Sciences*  
376 138:104655.
- 377 15 Ng TT, Zhou W, Chang XL (2017) Effect of particle shape and fine content on the behavior of

- 378 binary mixture. *Journal of Engineering Mechanics* 143:C4016008
- 379 16 Phan QT, Bui HH, Nguyen GD, & Bouazza A (2021) Effect of particle rolling resistance on  
380 drained and undrained behaviour of silty sand. *Acta Geotechnica* 1-26
- 381 17 Porcino DD, Diano V, Triantafyllidis T, & Wichtmann T (2020) Predicting undrained static  
382 response of sand with non-plastic fines in terms of equivalent granular state parameter. *Acta*  
383 *Geotechnica* 15:867-882
- 384 18 Rahman, M. M., & Dafalias, Y. F. (2022). Modelling undrained behaviour of sand with fines  
385 and fabric anisotropy. *Acta Geotechnica*, 17(6), 2305-2324.
- 386 19 Richart FE (1970) *Vibrations of soils and foundations*. Prentice Hall. Inc., Englewood Cliffs,  
387 New Jersey
- 388 20 Roscoe KH, Schofield A, Wroth AP (1958) On the yielding of soils. *Geotechnique* 8:22-53
- 389 21 Saberi M, Annan CD, Konrad JM (2017) Constitutive modeling of gravelly soil–structure  
390 interface considering particle breakage. *Journal of Engineering Mechanics* 143:04017044
- 391 22 Schofield AN, Wroth P (1968) *Critical state soil mechanics*. London: McGraw-hill Vol. 310
- 392 23 Shi XS, Liu K, Yin J (2021) Analysis of mobilized stress ratio of gap-graded granular  
393 materials in direct shear state considering coarse fraction effect. *Acta Geotechnica*  
394 6:1801-1814
- 395 24 Shi XS, Zhao JD, Gao YF (2021) A homogenization-based state-dependent model for gap-  
396 graded granular materials with fine-dominated structure. *International Journal for Numerical*  
397 *and Analytical Methods in Geomechanics* 45:1007-1028
- 398 25 Shi XS, Zhao JD, Yin JH, et al (2019) An elastoplastic model for gap-graded soils based on  
399 homogenization theory. *International Journal of Solids and Structures* 163:1-14
- 400 26 Sun, Z., Chu, J., & Xiao, Y. (2021). Formulation and implementation of an elastoplastic  
401 constitutive model for sand - fines mixtures. *International Journal for Numerical and*  
402 *Analytical Methods in Geomechanics*, 45(18), 2682-2708.
- 403 27 Thevanayagam S (2007) Intergrain contact density indices for granular mixes—I: Framework.  
404 *Earthquake engineering and engineering vibration* 6:123
- 405 28 Thevanayagam S, Mohan S (2000) Intergranular state variables and stress–strain behaviour of  
406 silty soils. *Geotechnique* 50:1-23
- 407 29 Wang T, Liu SH, Wautier A, Nicot F (2022) An updated skeleton void ratio for gravelly sand  
408 mixtures considering the effect of grain size distribution. *Canadian Geotechnical Journal*,  
409 59(1): 12-23.
- 410 30 Wang T, Wautier A, Liu SH, Nicot F (2021) How fines content affects granular plasticity of  
411 under-filled binary mixtures, *Acta Geotechnica*, 2021: 1-15.
- 412 31 Wang ZL, Dafalias YF, Shen CK (1990) Bounding surface hypoplasticity model for  
413 sand. *Journal of engineering mechanics* 116: 983-1001

- 414 32 Wautier A, Bonelli S, Nicot F (2019) Rattlers' contribution to granular plasticity and  
415 mechanical stability. *International Journal of Plasticity* 112:172-193
- 416 33 Vallejo LE (2021) Interpretation of the limits in shear strength in binary granular mixtures.  
417 *Canadian Geotechnical Journal* 38:1097-1104
- 418 34 Xiao Y, Sun YF, Hanif KF (2015) A particle-breakage critical state model for rockfill material.  
419 *Science China Technological Sciences* 58:1125-1136
- 420 35 Xiao Y, Sun YF, Liu HL, et al (2017) Model predictions for behaviors of sand-nonplastic-fines  
421 mixtures using equivalent-skeleton void-ratio state index. *Science China Technological*  
422 *Sciences* 60: 878-892
- 423 36 Xiong H, Yin Z Y, Zhao J, et al (2021) Investigating the effect of flow direction on suffusion  
424 and its impacts on gap-graded granular soils. *Acta Geotechnica* 16: 399-419
- 425 37 Xu WJ, Qiang X, Hu RL (2011) Study on the shear strength of soil–rock mixture by large  
426 scale direct shear test. *International Journal of Rock Mechanics and Mining Sciences*  
427 48:1235-1247
- 428 38 Yang YT, Sun GH, Zheng H, et al (2019) Investigation of the sequential excavation of a  
429 soil-rock-mixture slope using the numerical manifold method[J]. *Engineering Geology* 256:  
430 93-109
- 431 39 Yin ZY, Huang HW, Hicher PY (2016) Elastoplastic modeling of sand–silt mixtures. *Soils and*  
432 *Foundations* 56:520-532
- 433 40 Yin ZY, Zhao JD, Hicher PY (2014). A micromechanics-based model for sand-silt mixtures.  
434 *International journal of solids and structures* 51:1350-1363
- 435 41 Zhang G, Zhang JM, Yu Y (2007) Modeling of gravelly soil with multiple lithologic  
436 components and its application. *Soils and Foundations* 47:799-810
- 437 42 Zhao LH, Huang DL, Zhang SH, et al (2021) A new method for constructing finite difference  
438 model of soil-rock mixture slope and its stability analysis. *International Journal of Rock*  
439 *Mechanics and Mining Sciences* 138: 104605

440

## 441 **Appendix: Calibration of model parameters**

### 442 **(1) Elastic parameters**

443 The initial elastic shear modulus,  $G$ , can be obtained from the experimental data of deviatoric  
444 stress,  $q$ , versus the deviatoric strain,  $\varepsilon_s$  when the axial strain is lower than 0.2%. Rearrangement  
445 of Equation (10) gives:

$$G_0 = G \frac{(1+e)}{(2.97-e)^2 \sqrt{P' P_a}} \quad (\text{A1})$$

446 The values of the elastic constant,  $G_0$ , at various confining pressures, can be determined from

447 Equation (A1). The average value of  $G_0$  under different confining pressures is adopted.

448 Based on Equations (7)-(11), the Poisson's ratio,  $\nu$  can be obtained by:

$$\nu = \frac{9d\varepsilon_s^e - 2d\varepsilon_v^e}{18d\varepsilon_s^e + 2d\varepsilon_v^e} \approx \frac{9\varepsilon_s - 2\varepsilon_v}{18\varepsilon_s + 2\varepsilon_v} \quad (\text{A2})$$

#### 449 (2) Critical state parameters

450  $e_\Gamma$ ,  $\lambda$  and  $\xi$  can be determined by directly fitting the experimental data for the critical state

451 line. The critical state stress ratio  $M$  can be obtained by fitting critical state test data in  $p'$ - $q$  plane

452 with a function of  $q = Mp'$ .

#### 453 (3) Dilatancy parameters

454 The parameter  $m$  is determined from Equation (17) at a phase transformation state, at which

455  $D=0$ , and thus,

$$m = \frac{1}{\psi^d} \ln \frac{M^d}{M} \quad (\text{A3})$$

456 where  $\psi^d$  and  $M^d$  are the values of  $\psi$  and  $\eta$  at the phase transformation state.

457 Ignoring the small elastic strain, we have:

$$\frac{d\varepsilon_v}{d\varepsilon_q} \approx \frac{d\varepsilon_v^p}{d\varepsilon_q^p} = D = d_0 \left( \exp(m\psi) - \frac{\eta}{M} \right) \quad (\text{A4})$$

458 The parameter  $d_0$  is determined based on the  $d\varepsilon_v$ - $d\varepsilon_q$  curve.

#### 459 (4) Hardening parameters

460 The parameter  $n$  is determined by Equation (14) at a peak stress state, at which  $K_p=0$ :

$$n = \frac{1}{\psi^b} \ln \frac{M}{M^b} \quad (\text{A5})$$

461 where  $\psi^b$  and  $M^b$  are the values of  $\psi$  and  $\eta$  at the peak stress state.

462 Combining Equations (10) (13) and (14) for conventional drained tests ( $dp' = dq/3$ ) yields:

$$\frac{dq}{d\varepsilon_q} \approx \frac{dq}{d\varepsilon_q^p} = \frac{K_p}{1 - \eta/3} = h \left\{ \frac{G_0(2.97 - e)^2 \sqrt{p'p_a} \left( \frac{M}{\eta} - \exp(n\psi) \right)}{(1 + e)(1 - \eta/3)} \right\} \quad (\text{A6})$$

463 As all the model parameters in the brackets are known,  $h$  is determined based on  $dq - d\varepsilon_q$

464 curves along drained triaxial loading paths. Then parameters  $h_1$  and  $h_2$  can be obtained by

465 equation  $h = h_1 - h_2 e_0$ .